

PAPER • OPEN ACCESS

FLASH radiotherapy sparing effect on the circulating lymphocytes in pencil beam scanning proton therapy: impact of hypofractionation and dose rate

To cite this article: Antje Galts and Abdelkhalek Hammi 2024 *Phys. Med. Biol.* **69** 025006

View the [article online](#) for updates and enhancements.

You may also like

- [Adaptation and dosimetric commissioning of a synchrotron-based proton beamline for FLASH experiments](#)
Ming Yang, Xiaochun Wang, Fada Guan et al.
- [Modeling ultra-high dose rate electron and proton FLASH effect with the physicochemical approach](#)
Hai Siong Tan, Kevin Boon Keng Teo, Lei Dong et al.
- [Physics and biology of ultrahigh dose-rate \(FLASH\) radiotherapy: a topical review](#)
Nolan Esplen, Marc S Mendonca and Magdalena Bazalova-Carter



Joining forces:
One complete
QA solution for
Dosimetry with
myQA[®], QUASAR[™]
and Radcal[®]!



The diagram is a circular graphic with a dark background and a pattern of small, colorful dots. It consists of four colored segments arranged in a circle: a dark blue segment at the top left labeled 'Machine QA', a green segment at the top right labeled 'Patient Specific QA', a light blue segment at the bottom labeled 'Medical Imaging QA', and a pink segment at the center labeled 'Risk Management'. In the center of the pink segment is a white circle containing a green wireframe model of a human head and neck.



PAPER

OPEN ACCESS

RECEIVED
22 September 2023REVISED
6 December 2023ACCEPTED FOR PUBLICATION
11 December 2023PUBLISHED
5 January 2024

Original content from this work may be used under the terms of the [Creative Commons Attribution 4.0 licence](#).

Any further distribution of this work must maintain attribution to the author(s) and the title of the work, journal citation and DOI.



FLASH radiotherapy sparing effect on the circulating lymphocytes in pencil beam scanning proton therapy: impact of hypofractionation and dose rate

Antje Galts and Abdelkhalek Hammi

TU Dortmund University, Dortmund, Germany

E-mail: abdelkhalek.hammi@tu-dortmund.de**Keywords:** FLASH, proton therapy, radiation-induced lymphopenia, immune system, circulating blood

Abstract

Purpose. The sparing effect of ultra-high dose rate (FLASH) radiotherapy has been reported, but its potential to mitigate depletion of circulating blood and lymphocytes (CL) has not been investigated in pencil-beam scanning-based (PBS) proton therapy, which could potentially reduce the risk of radiation-induced lymphopenia. **Material and methods.** A time-dependent framework was used to score the dose to the CL during the course of radiotherapy. For brain patients, cerebral vasculatures were semi-automatic segmented from 3T MR-angiography data. A dynamic beam delivery system was developed capable of simulating spatially varying instantaneous dose rates of PBS treatment plans, and which is based on realistic beam delivery parameters that are available clinically. We simulated single and different hypofractionated PBS intensity modulated proton therapy (IMPT) FLASH schemes using 600 nA beam current along with conventionally fractionated IMPT treatment plan at 2 nA beam current. The dosimetric impact of treatment schemes on CL was quantified, and we also evaluated the depletion in subsets of CL based on their radiosensitivity. **Results.** The proton FLASH sparing effect on CL was observed. In single-fraction PBS FLASH, just 1.5% of peripheral blood was irradiated, whereas hypofractionated FLASH irradiated 7.3% of peripheral blood. In contrast, conventional fractionated IMPT exposed 42.4% of peripheral blood to radiation. PBS FLASH reduced the depletion rate of CL by 69.2% when compared to conventional fractionated IMPT. **Conclusion.** Our dosimetric blood flow model provides quantitative measures of the PBS FLASH sparing effect on the CL in radiotherapy for brain cancer. FLASH Single treatment fraction offers superior CL sparing when compared to hypofractionated FLASH and conventional IMPT, supporting assumptions about reducing risks of lymphopenia compared to proton therapy at conventional dose rates. The results also indicate that faster conformal FLASH delivery, such as passive patient-specific energy modulation, may further enhance the sparing of the immune system.

1. Introduction

Radiotherapy for cancer can have both immunostimulatory and immunosuppressive effects with respect to the tumor (Allavena 2008). It can enhance immune cell infiltration and inhibit tumor growth (Ni 2012, Klug 2013), but also undermine the innate antitumor immunity by causing lymphopenia and promoting tumor growth (Allavena 2008, Aymeric and Apetoh 2010). Recent clinical evidence links radiotherapy-induced lymphopenia with poor outcomes in cancer patients (Wu 2014, Diehl 2017, Cho 2019, Kleinberg 2019). In addition, correlations have been found between the severity of radiation-induced lymphopenia and the dose to the circulating blood cells and lymphocytes (CL), suggesting that minimizing dose exposure to the heart, PB, and lymphoid organs can mitigate this effect (Diehl 2017, Contreras 2018, Chen 2022). To address this issue and to widen the therapeutic window of radiotherapy, delivery protocol optimization and novel treatment schemes are required.

FLASH radiotherapy, characterized by an ultra-high dose rate ($>40 \text{ Gy s}^{-1}$), has demonstrated remarkable preservation of normal tissues and retention of antitumor efficacy in pre-clinical studies (Favaudon 2014, Montay Gruel 2017, Schüler 2017, Montay Gruel 2019, Vozenin 2019) and in the first application on a human patient (Bourhis 2019). Although electron beams were predominantly used in these investigations, recent studies have increasingly focused on proton FLASH radiotherapy (Patriarca 2018, Buonanno 2019, Diffenderfer 2020, Cunningham 2021, Nesteruk 2021). Especially since modern proton accelerators are designed to generate high-intensity proton beams, ultra-high dose rate administration of proton therapy is becoming increasingly feasible (Jolly 2020). In this regard, proton FLASH pencil beam scanning (PBS), with spatially and temporally varying dose rate, offers a promising avenue to mitigate the extent of radiation-induced lymphopenia. By reducing CL cells exposure time to radiation, it might spare the immune system more effectively compared to conventional fractionated PBS proton therapy (Durante 2018), such as intensity-modulated proton therapy (IMPT).

Because the etiology of radiation-induced lymphopenia is currently not well understood, a consensus regarding appropriate dosimetric constraints that might trigger such radiation-induced lymphopenia is elusive. This stems from the unavailability of tools enabling the calculation of the dose absorbed by CL (Yovino 2013, Hammi 2020). Furthermore, up to now there is no model that allows explicitly estimating dose to CL cells while both tracking the propagation of each individual blood particle and the time-dependent FLASH Bragg peak delivery, based on realistic beam delivery parameters available clinically today.

We recently developed a 4D computational framework that enables the estimation of the dose to the CL during time-dependent radiation field delivery of IMRT-based treatment plans by simulating the blood flow during radiotherapy delivery and thereby determining the dose delivered to CL during the radiotherapy treatment (Hammi 2023). The dosimetric blood flow model mimics the human circulatory system by simulating the spatiotemporal distribution of blood particles based on the hemodynamics references of the International Commission on Radiological Protection (ICRP89 2002).

The aim of this study was to develop a dosimetric framework enabling evaluation of the potential benefits of conformal PBS FLASH, in terms of sparing of CL in the PB, and comparison with hypofractionated FLASH schemes, as well as conventional fractionated IMPT treatment plans. For brain cancer patients, this study aimed to create a realistic cerebrovascular architecture from Magnetic Resonance Angiography (MRA) scans to simulate the spatiotemporal flow of blood and CL cells in the brain.

2. Materials and methods

2.1. Hybrid cerebrovascular model

2.1.1. Realistic arterial and venous system

The brain MRA images used in this study were obtained from a 3T scanner with a 3D gradient echo time-of-flight sequence (Wright 2013). The major arterial trees were segmented from the images providing a comprehensive overview of the six major arteries stemming from the circle of Willis, including the anterior cerebral arteries (ACAs), middle cerebral arteries (MCAs), and posterior cerebral arteries (PCAs) (see figure 1) (Brown 2005). We semi-automatically delineated the venous system to complete the cerebral vasculature model (see figure 2(a)), and then employed the multiple topographic blood pathlines methodology to trace optimal blood particles (BP) flow trajectories (Hammi 2023). This approach enables reconstructing of the intricate bifurcation network and probabilistic stream trajectories stemming from segmented major vessels (see figures 2(b)–(c)).

2.1.2. High-resolution cerebrovascular architecture: vascular fractal

A major challenge in developing a comprehensive model of the brain's blood vascular system is replicating the hierarchical branching structure of both arteries and veins, including their connecting junctions, while ensuring an overall perfusion throughout the entire brain without excess or deficiency. To address this challenge, we propose an approach that involves generating vascular structures using fractal-like branching. In this model, first the brain volume was divided into $N_T = 320$ vascular territories $T_d^v = \{T_1^v, T_2^v, \dots, T_{N_T}^v\}$. A vascular territory was conceptualized as a tetrahedral region nourished by the macroscopic artery vessel located within it. The vascular territories serve as the spatial boundary for the arborization starting points (see figure 2(d)). For each vascular territory T_d^v , a random terminal vertex is chosen from $v_{k,T_d^v}^i = \{v^1, v^2, \dots, v^n\}$, which is to serve as the bifurcation for generating new fractal arborizations, where i and k are the indices of the vertex and the corresponding vessel, respectively, and n is the counts of vertices. A new root vertex $v_{T_d^v}^{n+1}$ is randomly added to T_d^v , where the distance $\|v_{T_d^v}^{n+1} v_{k,T_d^v}^i\|$ is shorter than a threshold distance δ_d . A trunk is added to connect the $v_{T_d^v}^{n+1}$ and the macroscopic vessel at $v_{k,T_d^v}^i$. If the endpoints of all newly emerging branches are not situated within the

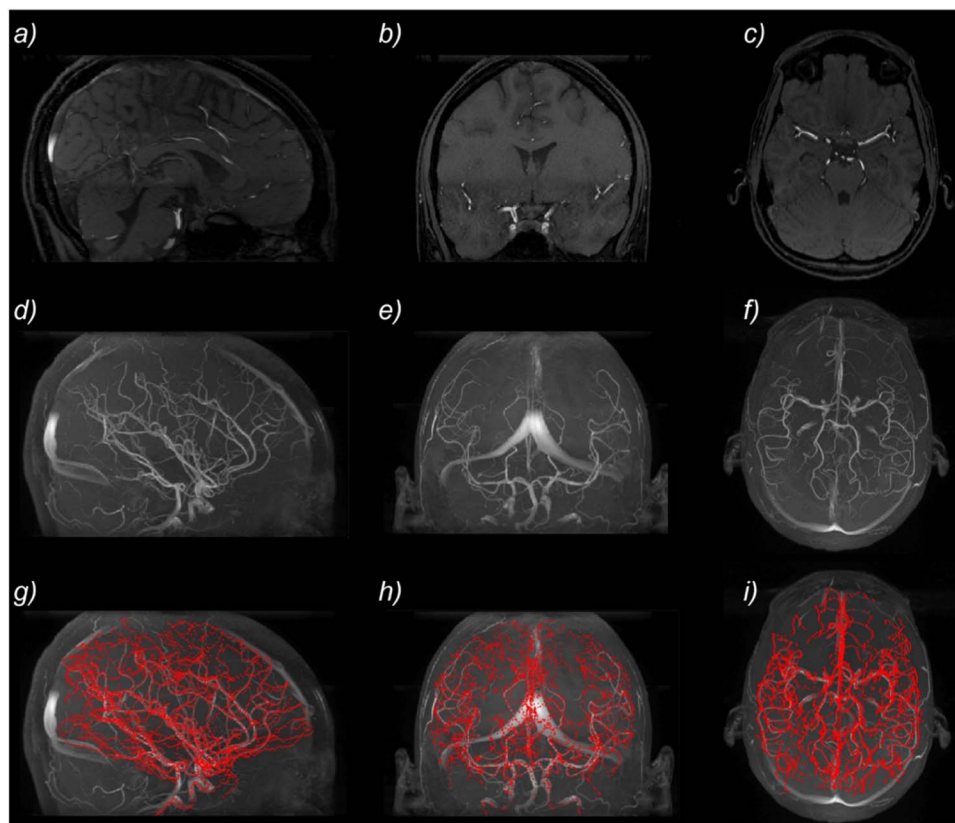


Figure 1. The workflow of blood vessel extraction from MRA data. Figures (a)–(c) depict planar sections of MRA images, while figures (d)–(f) show the reconstructed maximum intensity projections in the same directions as in (a)–(c). These projections display the full extent of the visible brain arteries. Finally, figures (g)–(i) illustrate segmented arterial branching overlaid on the reconstructed images of (d)–(f). Rows are arranged in lateral, posterior-anterior, and transversal orientations.

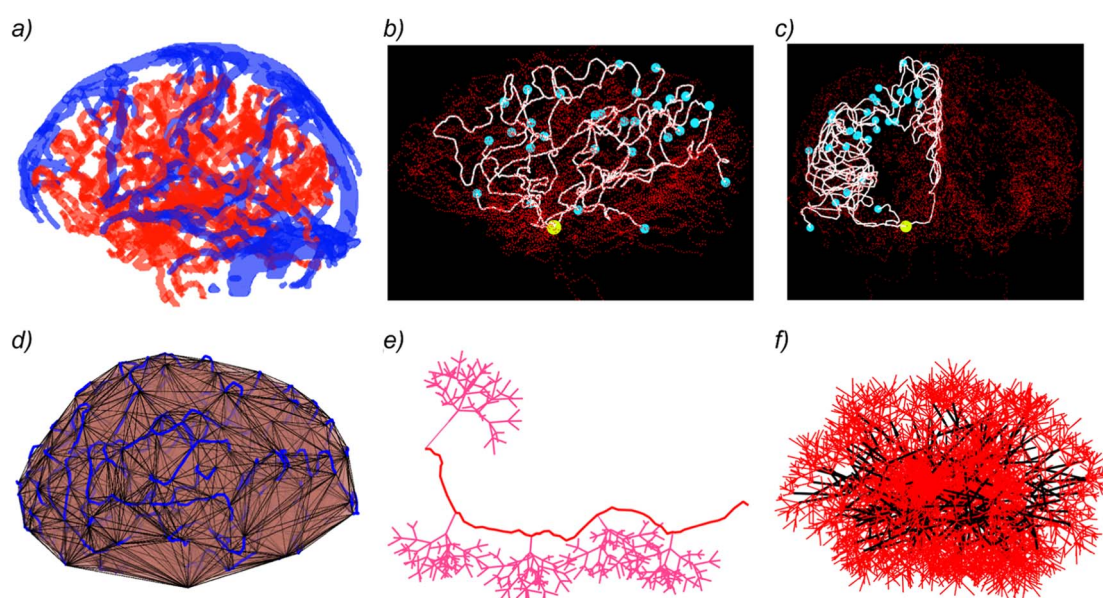


Figure 2. (a) Color-coded segmented arteries (red) and vein (blue). (b) Tracing blood pathlines (white lines) from skeletonized arteries (red nodes). Potential paths, originating from a single bifurcation (yellow sphere) and reaching different endpoints (cyan sphere). (c) Anterior-posterior orientations of (b). (d) Partitioning the brain into tetrahedrons sub-regions ('vasculature territories'). (e) Arborization of arterial pathway using fractal trees (pink). (f) A multi-generation cluster of fractals born from one fractal parent and composed of multiple clone daughters. Each daughter fractal is connected to its parent through a branch (black edges).

vascular territory, the current root is rejected, and a new vertex position is picked. The process is repeated until a suitable root terminal $v_{T_d}^{n+1}$ is identified. Then the parent vessel is bifurcated at v_{k,T_d}^i to guarantee blood supply to both the newly generated fractal and the previously perfused area of T_d^y (see figure 2(e)).

The vascular fractal $\xi_i(o, l_i, q, \alpha_o, R_i)$ is described by five parameters:

- The bifurcation order (o) refers to the cycle of the latest branch.
- The trunk length ($l_{i,o=0}$).
- The growth factor $q = l_{o+1}/l_o$ is the ratio of the Euclidian distance of two successive branches. It enables scaling up or down the vascular resolution.
- Vascular-branch tortuosity ($\alpha_i = \angle l_{o+1}^i l_o^i$) is the angular orientation in space of a daughter and parent branch. It provides a measure of how much the branches deviate from the centre path of the fractal.
- The reproducibility factor ($R_i = [r_1, r_2, r_3]$) sets the ability of fractal to grow its own hierarchical cluster trees by giving birth to other clone-fractals, where $r_1 = \begin{cases} 0 \\ b \end{cases}$ sets the clone fractal at the b th bifurcation of the parent fractal. If $r_1 = 0$, ξ_i will not contain any clones. r_2 is binary and it is determining whether the clone tree can expand by creating its own cluster of clones. r_3 establishes the resemblance between a parent fractal and its corresponding clone fractal (see figure 2(f)).

To maintain circulatory equilibrium in the brain, the blood volume entering the arteries must match the blood volume exiting the venous vessels. We generated capillary branches that established connections between the arteries and the nearest veins, ensuring that each arterial bifurcation point had at least one capillary link to a venous terminal end. Similarly, we constructed capillaries originating from vein endpoints. Capillaries which interconnected with adjacent vascular territories, including their connecting branch, were removed, and the blood flow in the parent vessels was adjusted to establish local equilibrium.

2.2. Treatment plan and dosimetric specification

A glioblastoma patient was randomly selected from the Glioma Image Segmentation for Radiotherapy study contained in the ‘The Cancer Imaging Archive’ (Clark 2013, Shusharina 2021). The clinical target volumes was 56.9 cm^3 . The open-source planning toolkit matRad Wieser (2017) was utilized for calculate the IMPT treatment plan for the patient. The IMPT plan was generated using four beam arrangements i.e. right antero-oblique, right posterior-oblique, left posterior-oblique and a superior-inferior beam coupled with treatment couch rotated at 90 degrees (see figure 3). The relative biological effectiveness (RBE) was set to 1.1.

Previous studies have suggested a fractionation for FLASH radiotherapy between 5–10 Gy per treatment fraction (Hornsey 1971, Favaudon 2014, Montay Gruel 2017). Krieger (2022) explored in their simulations dose per fractions ranging from 4.8–22.3 Gy fx^{-1} . While the optimal dose threshold for the FLASH normal tissue sparing effect is still under investigation, this study investigated three different FLASH fractionation schemes. The fraction dose was chosen to be equivalent to the biological equivalence dose of a reference fractionation of $30 \times 2 \text{ Gy}$, while accounting for a tumor α/β ratio of 10 Gy (see table 1).

2.3. Dynamic beam delivery

In the dynamic beam delivery simulations for PBS treatments, all pencil-beam energy layers were delivered at the full beam current (I_{Max}) of 2 nA during conventional IMPT (Hueso-González 2018) and 600 nA during FLASH radiotherapy (Jolly 2020). The spot delivery time (t_{spot}) was computed based on the intensity of the corresponding spot at its isocenter and I_{Max} (see figure 4(a)). Each spot’s current pulse was assumed to have a trapezoid shape. A generic current ramp-up period of $T_{\text{up}} = 200 \mu\text{s}$ was presupposed to achieve the maximum I_{Max} and a similar ramp-down $T_{\text{down}} = 200 \mu\text{s}$ (see figure 4(b)), corresponding to a theoretical minimum intensity of 2.49×10^6 protons for conventional IMPT. For FLASH delivery, a minimum intensity of 3.74×10^8 protons was considered. The lateral spot adjustment time of the spots ($T_{M_x, y}$) was calculated with a scanning speed of $M_x = 30 \text{ m ms}^{-1}$ and $M_y = 3 \text{ m ms}^{-1}$ for lateral and perpendicular deflection. The energy layer switching (ELS) time ($T_{\Delta E}$) was set to be invariant between the energy layers (van de Water 2019). $T_{\Delta E}$ corresponded to 2 s during conventional dose rate delivery mode. During the FLASH mode, we assumed a generic rapid $T_{\Delta E}$ of 0.01 s. The beam energy modulation step size was set at $\Delta E = 1.7 \text{ MeV}$, corresponding to a range modulation step of 1.8–4.2 mm water equivalent thickness at clinical energies (i.e. 70–230 MeV) (see figure 4). Proton gantry rotations and patient couch adjustments between beams (T_G) varied randomly between 30 s and 60 s.

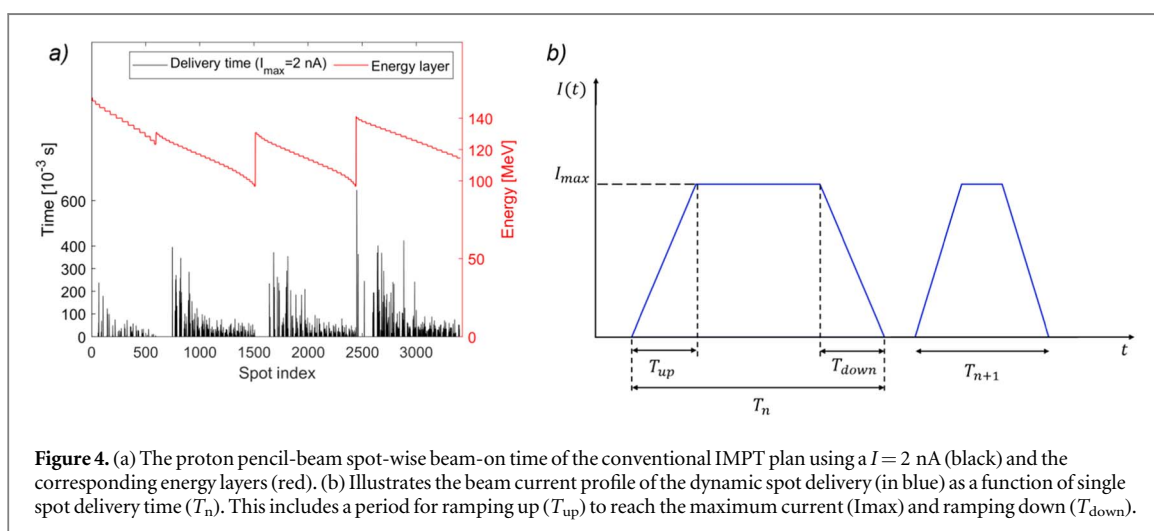
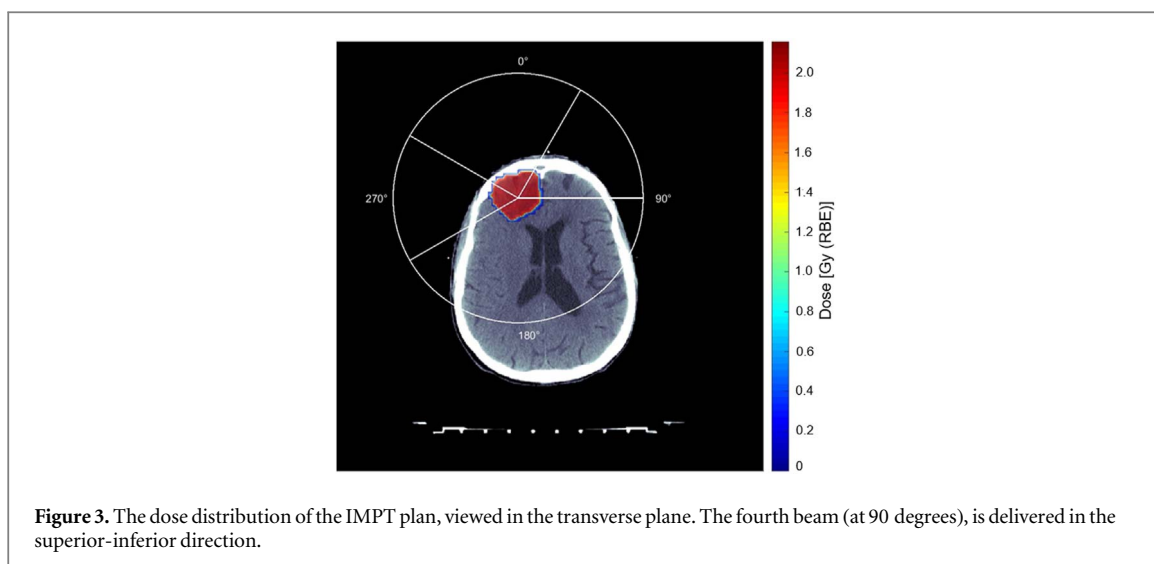


Table 1. The different fractionation schemes used in the study.

Scenario	Cyclotron current (nA)	Fraction scheme
Conventional IMPT	2	30×2 Gy
FLASH 1Fx	600	1×22.3 Gy
FLASH 2Fx	600	2×14.6 Gy
FLASH 5Fx	600	5×8 Gy

2.4. Dynamic simulation of the treatment delivery and dose scoring

The cerebral vascular model was co-registered to the CT coordinate system. The patient's heart rate was set to 65 bpm. The PB volume was assumed to be 5.6 l. The cardiac output was set to 6 l min^{-1} , corresponding to the adult reference person according to ICRP89 (ICRP89 2002). The PB of the model comprises 42.125×10^6 BP, with each BP having a volume of $1.25 \mu\text{l}$. The brain region contained 1.2% of the total blood volume. The regional volumes and flow rates of the circulatory system model were adopted from our previous model (for more details see (Hammi 2023)). We applied the transition probability approach proposed by Hammi (2023) to account for blood mixing, and to determine the spatial distribution of CL prior to the commencement of the subsequent treatment fraction. During radiotherapy delivery, the accumulated dose of the PB was calculated by tracking the propagation trajectory \vec{x} of individual BP i through the spatially varying instantaneous dose rate field $\dot{D}(\vec{x}, t)$:

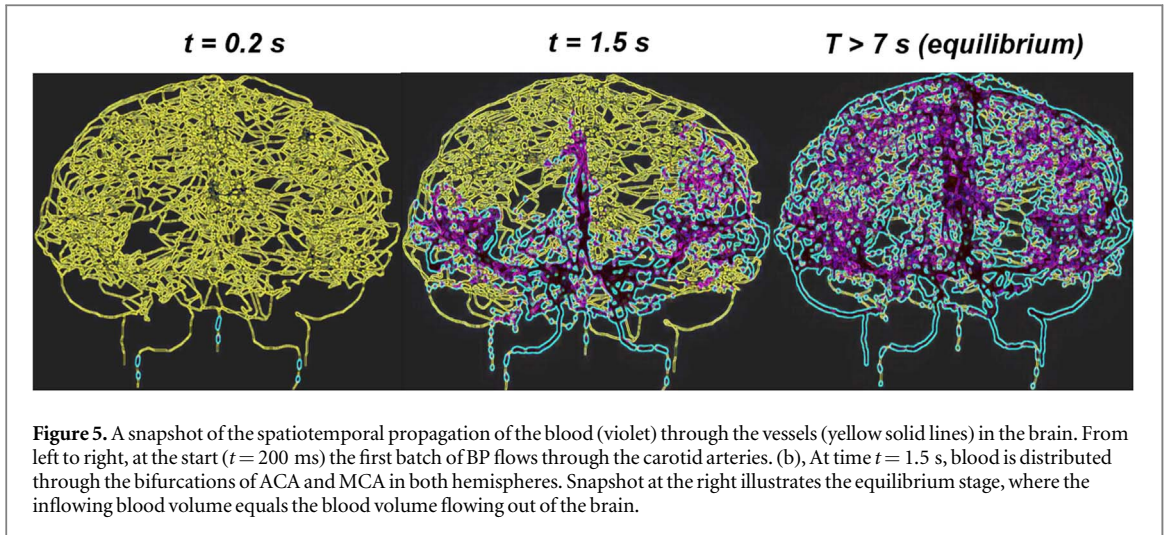


Figure 5. A snapshot of the spatiotemporal propagation of the blood (violet) through the vessels (yellow solid lines) in the brain. From left to right, at the start ($t = 200$ ms) the first batch of BP flows through the carotid arteries. (b), At time $t = 1.5$ s, blood is distributed through the bifurcations of ACA and MCA in both hemispheres. Snapshot at the right illustrates the equilibrium stage, where the inflowing blood volume equals the blood volume flowing out of the brain.

$$d_i^{F_n} = \sum_{j=1}^{F_n} \sum_{t=0}^{T_{F_j}} \dot{D}(\vec{x}, t) * \Delta t, \quad (1)$$

where F_n is the fraction number. T_{F_j} is the treatment time of the j th fraction. The time evolution resolution of the dosimetric blood flow model was $\Delta t = 200 \mu\text{s}$. For fractionated treatment ($F_n \geq 2$), $d_i^{F_j-1}$ is reset to zero under the assumption of either complete repair or cell death. The dosimetric tracking enables our model to investigate how both a single treatment fraction and multiple sessions over time affect the depletion of the CL.

We compared the radiotoxicity to CL among the treatment scenarios outlined in table 1. This assessment was based on the irradiated PB volume and on dose-volume histograms (DVHs) of the total PB volume. We evaluated various DVH parameters, including $D_{2\%}$, $V_{D=7\text{cGy}}$ and $V_{D=43\text{cGy}}$, which correspond to the lethal doses depleting the lymphocyte population by 2% and 10%, respectively (Nakamura 1990). Additionally, we calculated the fraction of CL killed.

$$k = \sum_i V_i (1 - \exp(-\alpha d_i - \beta d_i^2)), \quad (2)$$

where V_i is the CL partial volume receiving the dose d_i . α and β are radiosensitivity values of lymphocytes cell subsets. Since the distribution of CD4+ and CD8+ lymphocytes subpopulations in PB differs, we assessed their depletion individually in response to the different radiotherapy scenarios. For CD4+, we used $\alpha = 0.29 \text{ Gy}^{-1}$ and $\beta = 0.14 \text{ Gy}^{-2}$, while for CD8+ subset, $\alpha = 0.18 \text{ Gy}^{-1}$ and $\beta = 0.14 \text{ Gy}^{-2}$ for CD8+ subset (Nakamura 1990).

3. Results

Figure 5 illustrates a time-lapse sequence of BPs flowing through the reconstructed hybrid cerebrovascular model. The brain model features a total of 465 realistic blood vessels and a total of 8841 individual vessel branches, including fractal-like bifurcations and capillaries. For better illustration only about 10% of the blood vessels are displayed. The reconstructed arterial branches comprise the major vessels of the ACA, MCA, and PCA, which directly bifurcate from the vertebral and carotid arteries, as well as the circle of Willis. The venous system is divided into two components: the dural venous sinuses, which include the superior sagittal, transverse, and sigmoid sinuses, and the cerebral veins, which comprise the superficial venous vessels responsible for draining most of the cerebral cortex, connecting directly to the dural sinuses.

The blood flows from the carotid and vertebral arteries. At time $t = 1.5$ s, the first BP that followed the shortest cerebral vasculature path (i.e. the path line from the vertebral artery to the occipital sinus over the occipital lobe) has reached the right sigmoid sinus vein. The cerebral blood flow equilibrium stage is reached after 7 s.

Figure 6 depicts the cumulative dosimetric histogram of CL and the DVHs for the first fraction side by side with the entire treatment plans, respectively. All three FLASH fractionation schemes irradiated approximately 1.52% of the PB volume. This resemblance is evident in figure 6(a). In contrast, conventional IMPT treatment irradiated approximately 45% more of CL (2.18% of PB volume) during the first fraction of the treatment. At both lethal dose thresholds of 7 cGy and 43 cGy, which resulted in a 2% and 10% depletion of the lymphocyte population, respectively, the irradiated CL volumes were as follows for single-fraction, two-fraction, and five-fraction FLASH scenarios: (1.21%, 0.91%), (1.15%, 0.84%), and (1.05%, 0.72%), when compared to (1.14%,

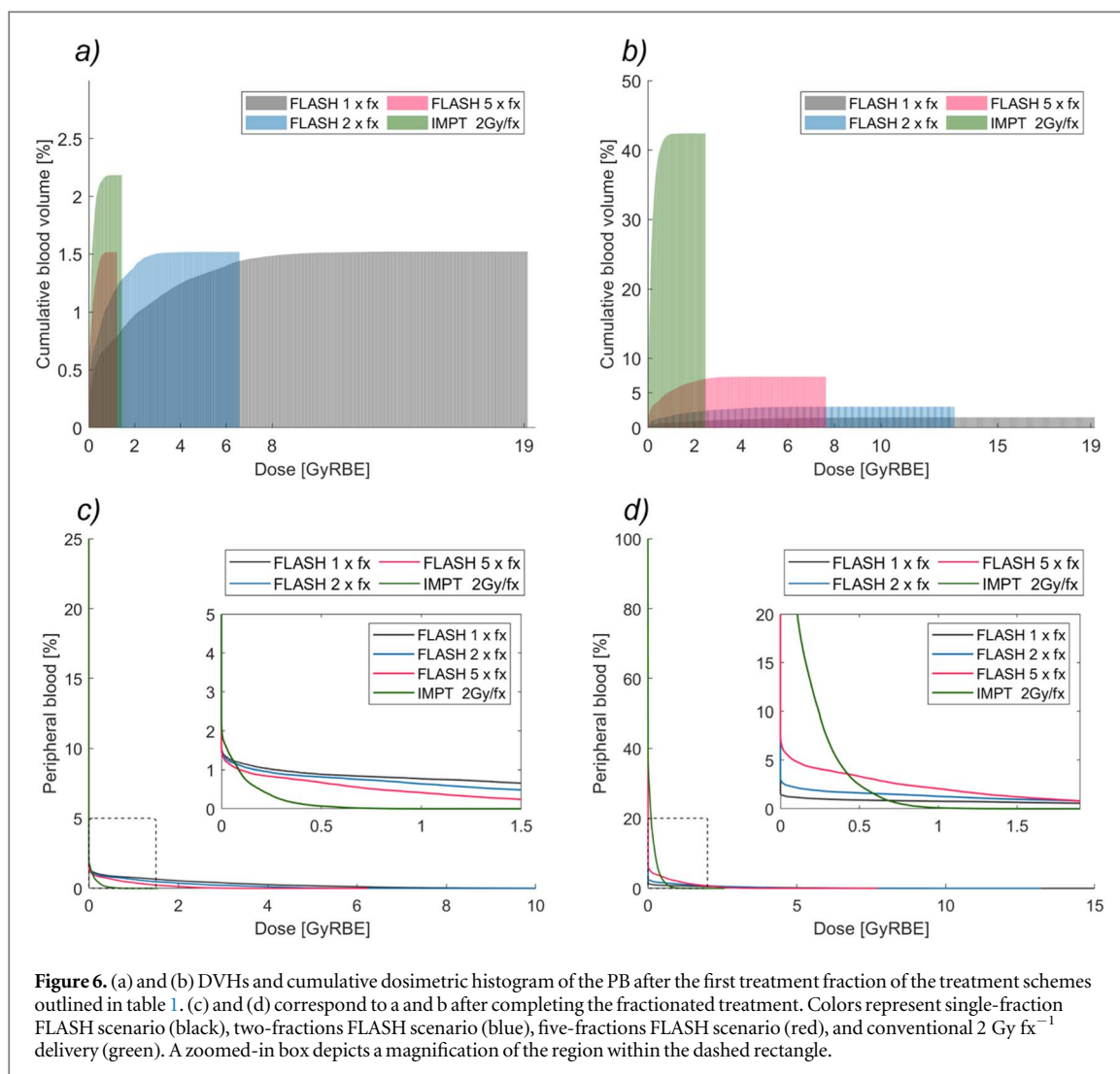


Figure 6. (a) and (b) DVHs and cumulative dosimetric histogram of the PB after the first treatment fraction of the treatment schemes outlined in table 1. (c) and (d) correspond to a and b after completing the fractionated treatment. Colors represent single-fraction FLASH scenario (black), two-fractions FLASH scenario (blue), five-fractions FLASH scenario (red), and conventional 2 Gy fx^{-1} delivery (green). A zoomed-in box depicts a magnification of the region within the dashed rectangle.

0.1%) for conventional IMPT. Hypofractionated FLASH treatment plans, when delivered in two and five fractions, significantly increased the volume of irradiated CL in PB compared to the single fraction FLASH scenario. The increase was 89% (3.01%) and 383.5% (7.35%), respectively. In contrast, conventional dose rate IMPT treatment plan irradiated 42.41% of the CL. After completing the conventional IMPT treatment, 25.65% of the CL received a dose of at least $D_{F_{30}} \geq 7 \text{ cGy}$, a lethal dose threshold causing a 2% depletion in the lymphocyte population. While the $V_{D>7\text{cGy}}$ was 1.21% 2.30% and 5.14% after completing the single, two, and five-fractions FLASH scenarios, respectively. For doses exceeding 100 cGy, which causes a 30% depletion in the lymphocyte population, the $V_{D>100\text{cGy}}$ were 0.77%, 1.28%, and 2.09% during the single-, two-, and five-fractions FLASH scenarios, respectively. The lowest irradiated volume $V_{D>100\text{cGy}}$ was 0.10% during the conventional IMPT treatment plan. The highest scored $D_{2\%}$ values of 0.16 Gy, 1.04 Gy and 0.54 Gy were observed over the course of two- and five-fractions FLASH scenarios and the conventional IMPT, respectively. The highest scored doses were 19.16 Gy, 13.15 Gy, 7.64 Gy, and 2.47 Gy for one-, two-, and five-fractions FLASH scenarios and conventional IMPT, respectively (see figure 6(b)).

Figures 7(a)–(b) shows the survival fraction spectra of CD4+ and CD8+ subsets during the different treatment delivery scenarios after the first fraction. The depletion during ultra-high dose rate treatments follows a sigmoid-curve form, while conventional dose rate delivery demonstrated a linear depletion. Cell killing of both for both CD4+ and CD8+ subsets were 0.66%, 0.62%, 0.32% and 0.08% during single- two- and five-fraction FLASH radiotherapy scenario as well as conventional dose rate IMPT, respectively. Figures 7(c) and (d) depict the CL survival fraction after completing the treatment. The CL depletion during FLASH radiotherapy varies with fractionation scheme. The survival fraction over single-fraction FLASH exhibited the highest slope. Escalating the fractionation of hypofractionated FLASH increased the absolute CL depletion to 1.02% and 1.56% for two- and five-treatment fractions, respectively. The survival fraction of conventional IMPT demonstrated a linear shape and depletes 2.14 of the CL%.

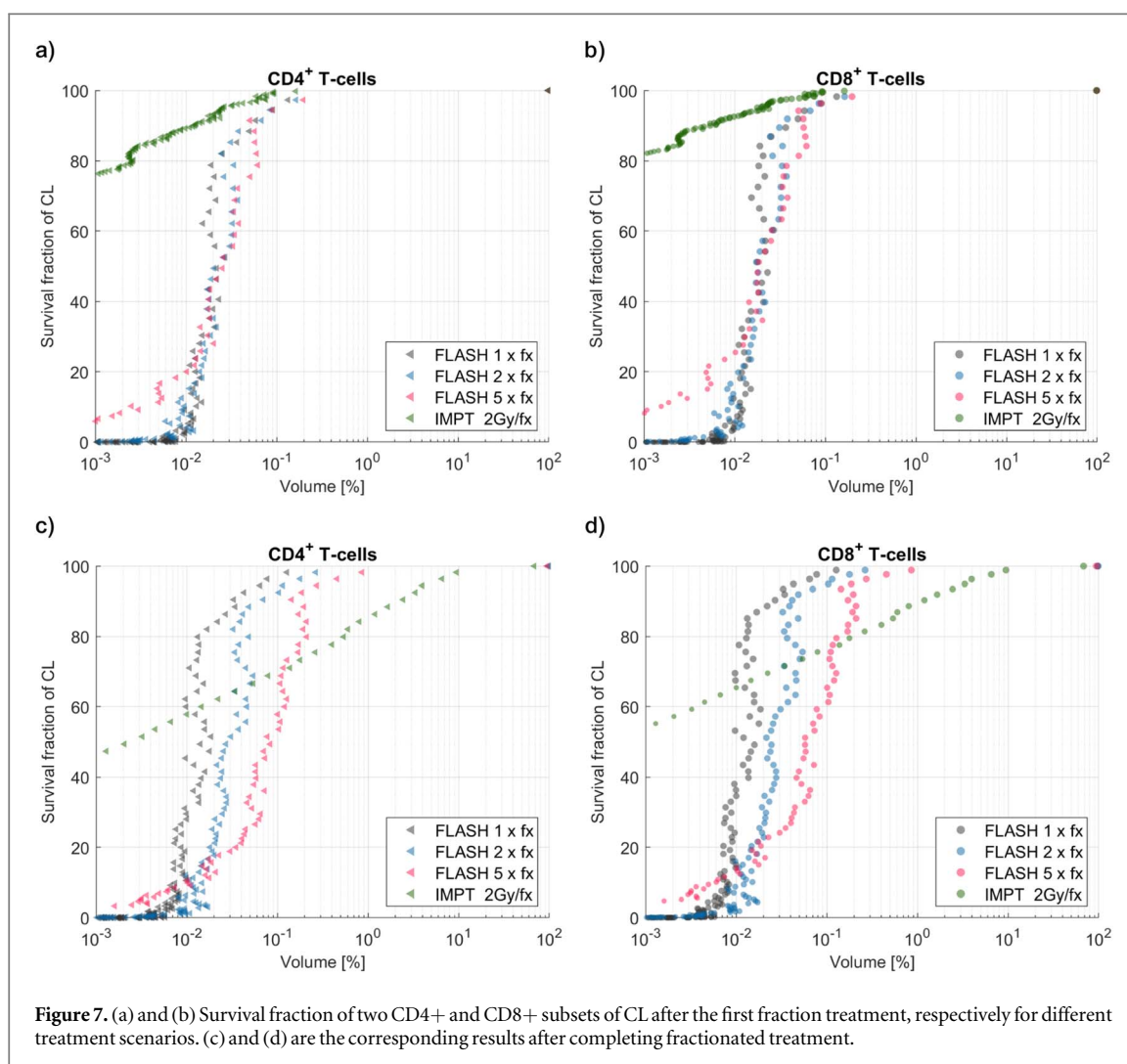
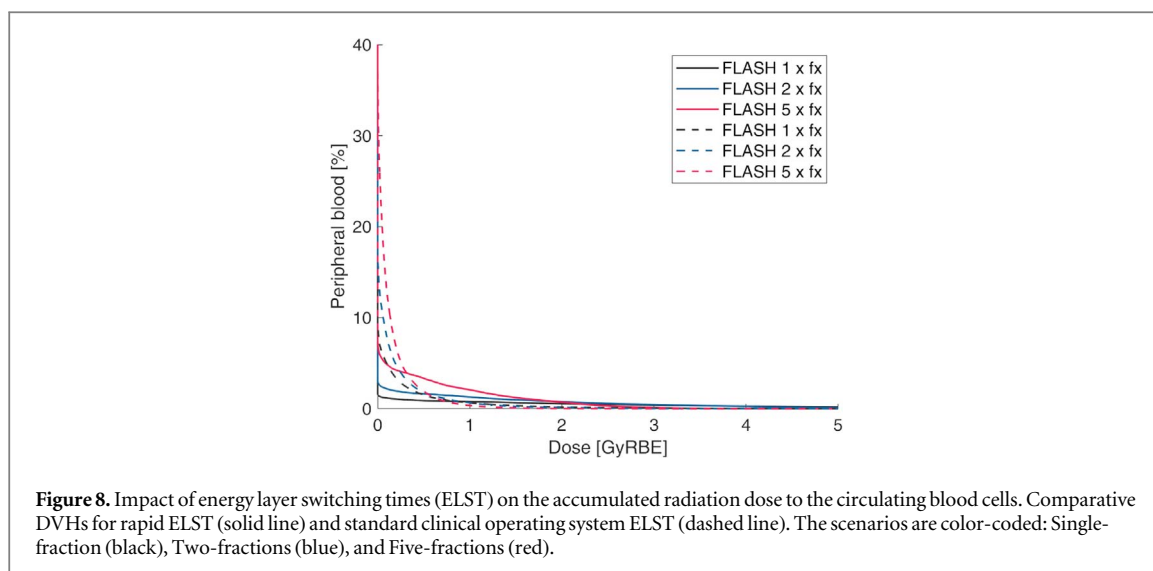


Figure 7. (a) and (b) Survival fraction of two CD4⁺ and CD8⁺ subsets of CL after the first fraction treatment, respectively for different treatment scenarios. (c) and (d) are the corresponding results after completing fractionated treatment.

4. Discussion

A framework was developed that models the immune cells circulation within the vascular blood stream of the irradiated organ, simulates realistic PBS delivery parameters used in clinical settings and estimates the depletion of lymphocytes caused by radiation throughout the course of radiotherapy. The cerebrovascular model accurately replicated the complex branching architecture of cerebral arteries and veins in the human brain, leading to a more precise representation of blood circulation in brain cancer patients and, thus, a more accurate radiation dose estimation (Hammi 2023). Additionally, the model considered the geographical distribution of the arborization of the main cerebral vessels as well as the corresponding vascular territories, a critical factor for Glioblastoma patients whose tumors extensively span one hemisphere of the brain. Moreover, the model allowed for flexible generation of sub-millimeter or coarse arborization models through the proposed fractal tree vascular generator. This opens up possibilities for a range of applications.

This study is the first computational analysis comparing the sparing effect of PBS FLASH on CL versus the PBS conventional dose rate deliveries. This study considers realistic clinical delivery parameters and the architecture of brain blood vessels. While irradiating only a portion of the brain, the single-fraction FLASH scenario led to an exposure of 1.5% of the circulating blood volume to radiation. This irradiated volume is approximately 30% larger than the total blood volume within the entire brain at a given time, despite the ultra-high dose rate and the resulting active delivery time of less than 0.2 s. Even so, further escalation of the dose rate will not notably impact the irradiated volume of the CL due to the effective dose rate saturation effect. This is primarily due to the retardation of the delivery caused by the speed of the ELS system. Therefore, conformal proton FLASH radiotherapy, which involves using a single treatment field without active ELS, such as passive energy modulation based on patient-specific ridge filters (Liu and Charyyev 2023) or treatment deliveries with single, alternating fields (Rothwell and Lowe 2022), holds promising potential for reducing radiation exposure to CL.



The FLASH radiotherapy significantly reduced the proportion of irradiated CL cells in comparison to conventional dose rate IMPT. This difference could potentially elucidate the underlying mechanism behind the observed FLASH effect (Durante 2018) while also suggesting a prospective enhancement in tumor control (Shukla 2023). This is particularly noteworthy given the reported correlation between radiation-induced lymphopenia and overall survival in different cancer indications that undergo radiotherapy (Contreras 2018, Cho 2019, Abravan 2020, Upadhyay 2021, Chen 2022). Therefore, considering the immune system as an organ at risk during radiotherapy can offer significant benefits to thoracic patients. This is because a considerable portion of their PB is exposed to radiation, given the proximity of vital structures such as the heart and major blood vessels to the treatment target. The dynamic blood flow model used in this study already incorporates blood flow through both the pulmonary circuit and primary lymphoid organs (the thymus and bone marrow) (Hammi 2023). In the context of evaluating immunotoxicity caused by fractionated radiotherapy with highly dynamic deliveries, such as IMPT, additional adjustments are required for accurately scoring the dose to the CL. These adjustments should encompass a detailed vascular cartography of the pulmonary circuit, considerations for the motion of the heart ventricles, and the thoracic duct vessel, which connects to the bloodstream. Furthermore, it is crucial to consider the bidirectional migration of immune cells residing in the lymphatic system, representing approximately 95% of the total immune cell population. This migration occurs through primary lymphoid organs and secondary lymphoid organs (including lymph nodes, spleen, and tonsils), as well as non-lymphoid organs such as the lungs, liver, and PB.

Although irradiated volume of CL is reduced in FLASH radiotherapy scenarios, the effective killing rate (ratio of the CL volume killed to the volume of CL irradiated) is notably higher when compared to conventional dose rate treatment. Specifically, the effective killing rates were 45%, 35%, 23%, and 5% for single-, two-, and five-fraction FLASH scenarios, as well as conventionally fractionated IMPT, respectively. This highlights the relationship between the volume of CL cells receiving a small dose and the highest absorbed dose, which depends on the fractionation scheme as well as the effective dose rate (Hammi 2020, 2023). This cell killing during FLASH scenarios however was calculated using the LQ-model, which was adapted from conventional dose rate measurements (Nakamura 1990), as the proper LQ-model for ultra-high dose rates remains not available.

In our study, we considered parameters of commercially available cyclotrons and realistic beam deliveries to simulate more realistic dynamic beam delivery. However, we deliberately excluded considerations related to safety and beam monitoring restrictions. Instead, we assumed rapid ELS capabilities of $T_{\Delta E} = 10$ ms, to achieve an effective ultra-high dose rate exceeding 40 Gy s^{-1} . It is important to highlight that the ELS systems in most clinical operations have slower ELS times, taking more than 500 ms to change between energy steps. Consequently, using such clinical ELS times would prolong the fraction delivery time for the FLASH scenarios considered in this study, subsequently reducing the fraction time weighted dose rate of treatment fractions [see reference 2023]. Figure 8 illustrates the impact of using a slower ELS time of $T_{\Delta E} = 750$ ms on the final dose distribution to the circulating blood cells in the same treatment scenarios discussed earlier. As $T_{\Delta E}$ increases, the fraction of CL irradiated also increases, to 9%, 17.2%, and 37.6% for one-, two-, and five-fraction FLASH treatments scenario, respectively. Simultaneously, this leads to a reduction in the $D_{1\%}$ to 0.7 Gy, 0.8 Gy, and 0.67 Gy for one-, two-, and five-fraction FLASH treatments, respectively. Nevertheless, assuming rapid ELS in the dynamic beam delivery simulations do not impact the results, if the concept of FLASH persistence time is

considered, which suggests that the FLASH effect could still be observed in the irradiated region for a short period after irradiation (Mazal 2020).

Our blood flow model considers only the CL, comprising approximately 5% of the overall lymphocyte population. It also does not incorporate the migration between the lymphatic system and the blood, as the majority of lymphocytes primarily reside in the spleen and lymph nodes (Blum 2007). Nevertheless, considering the absence of lymphatic tissues in the brain, our analysis for intracranial irradiation can be confined to assessing the dose received by CL.

5. Conclusion

In this study, we investigated the impact of FLASH Bragg peak and conventional fractionated IMPT on circulating immune cells. The findings revealed that FLASH proton therapy, especially when delivered using a single treatment fraction, spares the circulating immune cells during intracranial treatment. Additionally, conformal FLASH treatments based on passive patient-specific energy modulation, without the need for energy switching or alternating single field treatments, may offer even greater immune system protection. Our results depend solely on quantitative dosimetric evaluation and remain irrespective of the mechanisms underlying the reported FLASH effect.

Acknowledgments

The authors express their sincere gratitude to Dr Fernando Hueso González, Dr Nadya Shusharina and Dr Sebastian Tattenberg for their insightful feedback and valuable input to this work.

Data availability statement

The data cannot be made publicly available upon publication because they are owned by a third party and the terms of use prevent public distribution. The data that support the findings of this study are available upon reasonable request from the authors.

Conflict of interest statement

The authors have no relevant conflicts of interest to disclose.

ORCID iDs

Abdelkhalek Hammi  <https://orcid.org/0000-0002-4001-1180>

References

- Abrahan A F-F 2020 Radiotherapy-related lymphopenia affects overall survival in patients with lung cancer *J. Thorac. Oncol.* **15** 1624–35
- Allavena P S 2008 The Yin-Yang of tumor-associated macrophages in neoplastic progression and immune surveillance *Immunol. Rev.* **222** 155–61
- Aymeric L and Apetoh L 2010 Tumor cell death and ATP release prime dendritic cells and efficient anticancer immunity *Cancer Res.* **70** 855–8
- Blum K S 2007 Lymphocyte numbers and subsets in the human blood Do they mirror the situation in all organs? *Immunol. Lett.* **108** 45–51
- Bourhis J S 2019 Treatment of a first patient with FLASH-radiotherapy *Radiother. Oncol.* **139** 18–22
- Brown K M 2005 A cross-platform freeware tool for digital reconstruction of neuronal arborizations from image stacks *Neuroinformatics* **3** 343–60
- Buonanno M G 2019 Biological effects in normal cells exposed to FLASH dose rate protons *Radiother. Oncol.* **139** 51–5
- Chen F J 2022 Radiation induced lymphopenia is associated with the effective dose to the circulating immune cells in breast cancer *Front. Oncol.* **12** 768956
- Cho Y P 2019 Impact of treatment-related lymphopenia on immunotherapy for advanced non-small cell lung cancer *Int. J. Radiat. Oncol. Biol. Phys.* **105** 1065–73
- Clark K V 2013 The cancer imaging archive (TCIA): maintaining and operating a public information repository *J. Digit. Imaging* **26** 1045–57
- Contreras J A 2018 Cardiac dose is associated with immunosuppression and poor survival in locally advanced non-small cell lung cancer *Radiother. Oncol.* **128** 498–504
- Cunningham S M 2021 FLASH proton pencil beam scanning irradiation minimizes radiation-induced leg contracture and skin toxicity in mice *Cancers* **13** 1012
- Diehl A Y 2017 Relationships between lymphocyte counts and treatment-related toxicities and clinical responses in patients with solid tumors treated with PD-1 checkpoint inhibitors *Oncotarget* **8** 114268–80

- Diffenderfer E S-M 2020 Design, implementation, and *in vivo* validation of a novel proton FLASH radiation therapy system *Biol., Phys.* **106** 440–8
- Durante M B-K 2018 Faster and safer? FLASH ultra-high dose rate in radiotherapy *Br. J. Radiol.* **91** 20170628
- Favaudon V C 2014 Ultrahigh dose-rate FLASH irradiation increases the differential response between normal and tumor tissue in mice *Sci. Transl. Med.* **6** 245ra93
- Hammi A 2023 4D dosimetric–blood flow model: impact of prolonged fraction delivery times of IMRT on the dose to the circulating lymphocytes *Phys. Med. Biol.* **68** 145017
- Hammi A P 2020 4D blood flow model for dose calculation to circulating blood and lymphocytes *Phys. Med. Biol.* **65** 055008
- Hornsey S 1971 Hypoxia in mouse intestine induced by electron irradiation at high dose-rates *Int. J. Radiat. Biol. Relat. Stud. Phys., Chem. Med.* **19** 479–83
- Hueso-González F R 2018 A full-scale clinical prototype for proton range verification using prompt gamma-ray spectroscopy *Phys. Med. Biol.* **63** 185019
- ICRP89 2002 Basic anatomical and physiological data for use in radiological protection reference values. A report of age- and gender-related differences in the anatomical and physiological characteristics of reference individuals. ICRP Publication 89 *Ann. ICRP* **32** 5–265 <https://pubmed.ncbi.nlm.nih.gov/14506981/>
- Jolly S O 2020 Technical challenges for FLASH proton therapy *Phys. Med.* **78** 71–82
- Kleinberg I S 2019 Radiotherapy, lymphopenia, and host immune capacity in glioblastoma: a potentially actionable toxicity associated with reduced efficacy of radiotherapy *Neurosurgery* **85** 441–53
- Klug F P-W 2013 Low-dose irradiation programs macrophage differentiation to an iNOS(+)/M1 phenotype that orchestrates effective T cell immunotherapy *Cancer Cell* **24** 589–602
- Krieger M V 2022 A quantitative FLASH effectiveness model to reveal potentials and pitfalls of high dose rate proton therapy *Med. Phys.* **49** 2026–38
- Liu R and Charyyev S 2023 An integrated physical optimization framework for proton stereotactic body radiation therapy FLASH treatment planning allows dose, dose rate, and linear energy transfer optimization using patient-specific ridge filters *Int. J. Radiat. Oncol. Biol. Phys.* **116** 949–59
- Mazal A P 2020 FLASH and minibeam in radiation therapy: the effect of microstructures on time and space and their potential application to protontherapy *Br. J. Radiol.* **93** 20190807
- Montay Gruel P A 2019 Long-term neurocognitive benefits of FLASH radiotherapy driven by reduced reactive oxygen species *PNAS* **116** 10943–51
- Montay Gruel P P 2017 Irradiation in a flash: unique sparing of memory in mice after whole brain irradiation with dose rates above 100 Gy s⁻¹ *Radiat. Oncol.* **124** 365–9
- Nakamura N K 1990 Radiosensitivity of CD4 or CD8 positive human T-lymphocytes by an *in vitro* colony formation *Radiat. Res.* **123** 224–7
- Nesteruk K P 2021 Commissioning of a clinical pencil beam scanning proton therapy unit for ultra-high dose rates (FLASH) *Med. Phys.* **48** 4017–26
- Ni J M 2012 Sustained effector function of IL-12/15/18-pretreated NK cells against established tumors *J. Exp. Med.* **209** 2351–65
- Patriarca A F 2018 Experimental set-up for FLASH proton irradiation of small animals using a clinical system *Biol., Phys.* **102** 619–26
- Rothwell B and Lowe M 2022 Treatment planning considerations for the development of FLASH proton therapy *Radiother. Oncol.* **175** 222–30
- Schüler E T 2017 Experimental platform for ultra-high dose rate FLASH irradiation of small animals using a clinical linear accelerator *Biol., Phys.* **97** 195–203
- Shukla S 2023 Ultra-high dose-rate proton FLASH improves tumor control *Radiother. Oncol.: J. Eur. Soc. Ther. Radiol. Oncol.* **186** 109741
- Shusharina N, Bortfeld T, Cardenas C, De B, Diao K, Hernandez S, Liu Y, Maroongroge S, Söderberg J and Soliman M 2021 Cross-modality brain structures image segmentation for the radiotherapy target definition and plan optimization *Segmentation, Classification, and Registration of Multi-modality Medical Imaging Data International Conference on Medical Image Computing and Computer-Assisted Intervention* vol 12587 (Lima, Peru, 4-8, October, 2020) pp 3–15
- Upadhyay R V 2021 Risk and impact of radiation related lymphopenia in lung cancer: a systematic review and meta-analysis *Radiother. Oncol.* **157** 225–33
- Vozenin M C 2019 The advantage of FLASH radiotherapy confirmed in mini-pig and cat-cancer patients. clinical cancer research *Cancer Res.* **25** 35–42
- van de Water S S 2019 Towards FLASH proton therapy: the impact of treatment planning and machine characteristics on achievable dose rates *Acta Oncol.* **58** 1463–9
- Wieser H P 2017 Development of the open-source dose calculation and optimization toolkit matRad *Med. Phys.* **44** 2556–68
- Wright S N 2013 Digital reconstruction and morphometric analysis of human brain arterial vasculature from magnetic resonance angiography *NeuroImage* **82** 170–81
- Wu C Y 2014 Enhanced cancer radiotherapy through immunosuppressive stromal cell destruction in tumors *Clin. Cancer Res.* **20** 644–57
- Yovino S K 2013 The etiology of treatment-related lymphopenia in patients with malignant gliomas: modeling radiation dose to circulating *Cancer Invest.* **31** 140–4